CO Chemisorption and Dissociation at High Coverages during CO Hydrogenation on Ru Catalysts

Brett T. Loveless,[†] Corneliu Buda,[‡] Matthew Neurock,*,[‡] and Enrique Iglesia*,[†]

[†]Department of Chemical and Biomolecular Engineering, University of California, Berkeley, California 94720, United States
[‡]Department of Chemical Engineering, University of Virginia, Charlottesville, Virginia 22904, United States

ABSTRACT: Density functional theory (DFT) and infrared spectroscopy results are combined with mechanism-based rate equations to assess the structure and thermodynamics of chemisorbed CO (CO*) and its activation during Fischer–Tropsch synthesis (FTS). CO* binding becomes weaker with increasing coverage on Ru(0001) and Ru_{201} clusters, but such decreases in binding energy occur at higher coverages on Ru_{201} clusters than on Ru(0001) surfaces (CO*/Ru = 1.55 to 0.75); such differences appear to reflect weaker repulsive interactions on the curved surfaces prevalent on small Ru_{201} clusters. Ru_{201} clusters achieve stable supramonolayer coverages (CO*/Ru > 1) by forming geminal dicarbonyls at low-coordination corner/ edge atoms. CO* infrared spectra on Ru/SiO_2 (~7 nm diameter) detect mobile adlayers that anneal into denser structures at saturation. Mechanism-based FTS rate equations give activation energies that reflect the CO*-saturated surfaces prevalent during catalysis. DFT-derived barriers show that CO* predominantly reacts at (111) terraces via H-assisted reactions, consistent with measured effects of H_2 and CO pressures and cluster size effects on rates and O-rejection selectivities. Barriers are much higher for unassisted CO* dissociation on (111) terraces and low-coordination atoms, including step-edge sites previously proposed as active sites for CO* dissociation during FTS. DFT-derived barriers indicate that unassisted CO* dissociation is irreversible, making such steps inconsistent with measured rates. The modest activation barriers of H-assisted CO* dissociation paths remove a requirement for special low-coordination sites for unassisted CO* activation, which is inconsistent with higher rates on larger clusters. These conclusions seem generally applicable to Co, Fe, and Ru catalysts, which show similar FTS rate equations and cluster size effects. This study also demonstrates the feasibility and relevance of DFT treatments on the curved and crowded cluster surfaces where catalysis occurs.
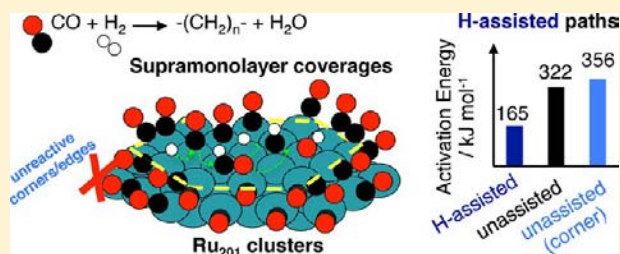
1. INTRODUCTION

Catalysis on supported metal clusters often occurs at conditions of near-saturation adsorbate coverages, for which coverages significantly influence the binding energies of adsorbed species and their reactivity in surface-catalyzed reactions. In alkane oxidation reactions, for example, changes in surface oxygen coverages cause sharp transitions in kinetic behavior and mechanisms.[1−3] High coverages favor reactions of intermediates with coadsorbed species instead of reactions involving vicinal vacant sites; for instance, O_2 dissociation on CO-covered Pt clusters occurs via direct reactions with adsorbed CO (CO*)[4] instead of O_2 reactions with vacant site pairs[5−7] during CO oxidation at low temperatures. CO hydrogenation to form large hydrocarbons (Fischer–Tropsch synthesis, FTS) also occurs on CO*-covered surfaces, as shown by previous kinetic,[8−11] infrared (IR) spectroscopic[12] and transient isotopic[13] data. The matter of whether C–O bonds are activated directly on vicinal vacant sites (*) or via reactions with coadsorbed hydrogen atoms (H*) in FTS reactions remains the subject of active debate and significant controversy. Here, we use density functional theory (DFT) and infrared studies to first assess the CO* coverages that prevail during FTS and then to probe the effects of CO* coverages on

adsorption energies and C–O bond activation paths on Ru clusters and extended Ru surfaces.

CO consumption rates in FTS reactions decrease strongly with decreasing cluster size on Co,[14] Fe,[15] and Ru[16] catalysts, indicating that low-coordination metal atoms, prevalent in small clusters,[17] are either less reactive than atoms with higher coordination in exposed low-index planes or that these low-coordination sites become unavailable because of strong interactions with adsorbed species during catalysis. In spite of these cluster size effects on FTS rates, several studies have proposed that low-coordination sites are required for direct CO dissociation during FTS reactions.[18−24] Direct CO dissociation routes are expected to be slow on CO*-covered surfaces, irrespective of the coordination of exposed metal atoms, because of the dearth of vacancies (*) during FTS reactions at the conditions of high H_2 and CO pressures required for hydrocarbon chain growth. CO* species are much more likely to reside vicinal to chemisorbed hydrogen atoms (H*) than to vacancies (*) because of high H_2 pressures and quasi-equilibrated H_2 adsorption during FTS reactions; as a result,

reactions of CO* with H* have been studied as an alternate CO activation route.[9,11,18,25−31] Such H-assisted routes allow facile CO dissociation on low-index planes of Co and Fe surfaces and are consistent with measured effects of H_2 and CO on FTS rates, with DFT simulations of direct and H-assisted dissociation reactions, and with the preferential formation of H_2O instead of CO_2 on these catalysts as the primary oxygen carrier.[9,10] FTS rate equations, oxygen rejection selectivities, and chain termination parameters[8,11,32] on Ru-based catalysts are similar to those found on Co, suggesting that H-assisted CO dissociation routes also prevail during FTS reactions on Ru cluster surfaces.

Theoretical treatments have been used previously to infer mechanistic details that are inaccessible to direct verification by experiments at the high reactant pressures required for significant chain growth in FTS.[18,21,24,33] These theoretical studies have invariably used extended surfaces with exposed low-index planes at CO* coverages well below saturation. These coverages ($CO*/M_{surface} < 0.75$) are consistent with the maximum coverages reported from thermal desorption studies of CO* on Co(0001)[34] and Ru(0001)[35] single crystals.

Repulsive intermolecular CO*-CO* interactions at high CO* coverages cannot be relieved on flat extended surfaces via lateral relaxation of adsorbed CO*,[31,36] as typically occurs on metal cluster surfaces with small domains of exposed crystal planes and convex shape.[4] Single crystals can accommodate high adsorbate coverages only via surface reconstruction,[19,37] whereas metal clusters stabilize high adsorbate coverages instead via relaxation of the surface adlayer itself. High adsorbate coverages weaken surface−adsorbate bonds;[4] these effects enhance the mobility of the adsorbed species involved in adlayer relaxation and avoid metal surface reconstruction otherwise required to stabilize high adsorbate coverages.

Here, we explore CO chemisorption on Ru clusters with 201 atoms (diameter = 1.8 nm, Ru_{201}) and containing exposed atoms of diverse coordination. These clusters can achieve monolayer (and even supramonolayer) CO* coverages and allow us to probe the effects of site coordination on the binding and reactivity of CO* on surfaces that represent working catalysts more faithfully than extended flat surfaces with CO* coverages well below one monolayer (ML). The effects of CO* coverage on the CO binding strength on these cluster surfaces are compared here with those on extended Ru(0001) surfaces to examine the roles of surface curvature, loosely defined by the differently oriented surface domains of small size, and binding site coordination on CO adsorption energies and CO* dissociation paths.

Ru_{201} cluster surfaces expose low-coordination atoms at corner and edge sites, and DFT treatments indicate that these atoms can interact with more than one CO* molecule which results in CO-to-surface atom ($CO*/Ru_s$, θ_{CO}) ratios significantly greater than unity. These ratios are consistent with the detection of high-frequency C−O stretching vibrations associated with Ru carbonyl species[38−40] on Ru/SiO_2 catalysts at near-saturation CO* coverages and with the known stability of Ru carbonyls.[41] DFT-derived activation energies for direct and H-assisted CO dissociation paths on CO*-covered Ru_{201} clusters at relevant CO* coverages are then used to assess the extent to which direct and H-assisted CO* dissociation paths contribute to FTS rates on Ru cluster surfaces. Our results show that CO* activation occurs primarily via H-assisted paths on high-coordination Ru atoms in CO*-covered (111) terraces of Ru_{201} cluster surfaces, consistent with FTS rate equations,

oxygen rejection selectivities, and cluster size effects on FTS rates; low-coordination sites are not necessary for CO* dissociation when H-assisted paths are available. Direct CO dissociation is unlikely to occur on high- or low-coordination Ru atoms at near-saturation CO* coverages and, in any case, is inconsistent with reported FTS rate equations.

2. THEORETICAL AND EXPERIMENTAL METHODS

2.1. Computational Procedures. Plane-wave, gradient-corrected periodic DFT calculations were carried out using the Vienna Ab initio Software Package (VASP)[42−44] with a plane-wave energy cutoff of 396 eV. All calculations used the revised Perdew−Burke−Ernzerhof (RPBE)[45] form of the generalized gradient approximation (GGA) and Vanderbilt ultrasoft pseudopotentials to describe the core−valence electron interactions.[46] The effects of CO* coverage on CO binding energies were investigated on flat two-dimensional extended Ru(0001) surfaces and on three-dimensional 201-atom Ru clusters (Ru_{201}), which expose atoms of different coordination and with potentially different adsorbate binding and catalytic properties. The face-centered cubic (fcc) arrangement of cuboctahedral Ru_{201} structures was used because it is the most stable configuration for Ru clusters with >140 atoms;[47] this cluster exposes surface atoms with coordination numbers ranging from six at corner sites to nine at (111) terraces.[17] As a result, Ru_{201} clusters seem well-suited to probe the effects of coordination on the binding and reactivity of chemisorbed CO.

Periodic Ru(0001) surfaces were treated as four layers of Ru atoms in a (3 × 3) unit cell. Adsorbed species and the uppermost two metal layers were fully relaxed, while the bottom two metal layers were fixed at an Ru−Ru distance of 0.2706 nm, estimated as the equilibrium distance by energy optimizations for bulk Ru lattices; these distances agree well with the lattice spacings measured in large Ru crystals (0.27058 nm).[48]

A (3 × 3 × 1) γ-centered k-point mesh was used to sample the first Brillouin zone for Ru(0001) surfaces; a single γ-centered k-point was used for the Ru_{201} cluster with a 25 × 25 × 25 Å³ unit cell that provided enough vacuum space to avoid interactions between the periodic cluster images. All atoms in the Ru_{201} cluster were allowed to relax until electronic energies varied by <1 × 10^{-4} eV, and the forces on all atoms were <0.05 eV Å^{-1}; these convergence criteria were deemed adequate, because a more stringent force convergence criterion (0.01 eV Å^{-1}) resulted in CO adsorption energies that were <2 kJ mol^{-1} different from those carried out using the initial (0.05 eV Å^{-1}) criterion on both the bare and CO*-covered Ru_{201} surfaces.

The structures and energies of reactants, products, and transition states were calculated for both direct and H-assisted CO* activation paths on (111) terraces of the Ru_{201} cluster. The activation energy for the direct path was also calculated on a Ru_{201} corner site as well as on a step-edge site that was formed by removing a row of Ru atoms at a (111) terrace edge to compare the reactivity of sites in low-coordination environments with terrace sites in highly coordinated environments. Terrace sites represent the majority of exposed atoms (75−78%) for clusters between 8 and 20 nm; in this size range, FTS turnover rates have been found to be essentially independent of cluster size for Ru[16,28] and Co[14,49] catalysts. Low-coordination sites, including step-edges, have been previously proposed as the sites required for direct CO dissociation on Co[19,21] and Ru[18,20] catalyst surfaces. Reactant and product states were calculated using the same methods and convergence criteria as for CO chemisorption on Ru_{201}; transition-state structures were isolated using the nudged elastic band (NEB)[50,51] and dimer methods.[52] A linear interpolation between reactant and product states was used to generate the initial path (8 or 16 images) for all NEB calculations. The highest energy structure along the converged NEB path was used as the initial guess for the transition-state structure, which was moved by the dimer method along the potential energy surface to a saddle point. Dimer convergence was achieved when the maximum force on any atom was <0.05 eV/Å and the structure was at a saddle point, as determined by a negative curvature of the two-dimensional reaction coordinate.

2.2. Catalyst Synthesis Procedures.

Silica-supported Ru catalysts (Ru/SiO_2) used in infrared studies of CO chemisorption were prepared using triethanolamine (TEA) ligands.[53] Ru(NO)-$(NO_3)_3$ (0.756 g, Alfa-Aesar, 32 wt % Ru) was dissolved in a solution of TEA (3.631 g Sigma Aldrich) in deionized H_2O (7.852 g) and added dropwise to SiO_2 gel (4.618 g, PQ Corp., CS-2133, 350 m^2 g^{-1}, 2.39 mL g^{-1}) to the point of incipient wetness. The SiO_2 was treated previously in flowing dry air (Praxair, extra-dry, 30 cm^3 (STP) s^{-1} g^{-1}) by heating to 773 K (at 0.083 K s^{-1}) and holding for 4 h. The resulting solids were treated in stagnant ambient air at 373 K for 10 h and then heated in flowing dry air (Praxair, extra dry, 30 cm^3 (STP) s^{-1} g^{-1}) to 673 K (at 0.0167 K s^{-1}) and held for 3 h. These samples were then cooled to ambient temperature and heated in a flowing 10% H_2/He mixture (Praxair, UHP, 50 cm^3 (STP) s^{-1} g^{-1}) to 673 K (at 0.0167 K s^{-1}) and held for 3 h. Samples were passivated by contact with a flowing stream of 0.1% O_2/He (Praxair, UHP, 50 cm^3 (STP) s^{-1} g^{-1}) stream at 303 K for 0.25 h before exposure to ambient air.

2.3. Infrared Spectra of CO Chemisorbed on Ru/SiO_2.

Catalyst samples were pressed into self-supporting wafers (30–50 mg cm^{-2}) and held within an infrared flow cell.[54] Infrared spectra were acquired using a Thermo Nicolet 8700 infrared spectrometer equipped with a HgCdTe (MCT) detector cooled with liquid N_2. Passivated samples were treated by heating to 598 K (at 0.083 K s^{-1}) in 30% H_2/He flow (Praxair, 5.0 grade, 20 cm^3 (STP) s^{-1} g^{-1}) and holding for 1 h. Samples were then cooled to ambient temperature in flowing He (Praxair, 5.0 grade, 10 cm^3 (STP) s^{-1} g^{-1}) and exposed to a flowing stream of 0.75% CO/He (Praxair, certified standard, 40 cm^3 (STP) s^{-1} g^{-1}) at ambient pressure to prepare CO*-saturated catalyst surfaces; CO*-saturation was confirmed by the invariance of the CO adsorption spectra with CO pressure (0.2–0.75 kPa). Absorbance spectra (4000–400 cm^{-1}, 4 cm^{-1} resolution) were obtained by averaging 16 scans per spectrum and subtracting a background spectrum (measured after the H_2/He treatments but before exposure to gaseous CO).

3. RESULTS AND DISCUSSION

3.1. CO* Coverage Effects on CO Binding Energies on Ru(0001) Surfaces.

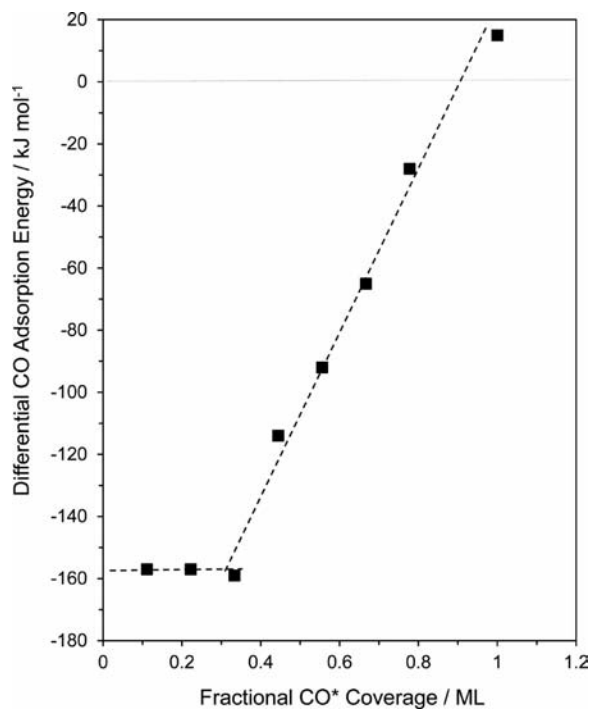Figure 1 shows the effects of increasing

Figure 1. Effect of fractional CO* coverage (adsorbed CO molecules per number of surface Ru atoms) on calculated differential CO adsorption energies for the 3 × 3 Ru(0001) surface.

fractional CO* coverages (adsorbed CO molecules per Ru surface atom, θ_{CO}) on differential CO adsorption energies estimated from DFT on 3 × 3 cells of Ru(0001) surfaces. The differential CO binding energy ($\Delta E_{CO,ads}$) is defined as

$$\Delta E_{CO,ads} = E_{Ru-CO_n} - E_{Ru-CO_{n-1}} - E_{CO_{(g)}} \quad (1)$$

Here, E_{Ru-CO_n} is the energy of the Ru surface with n CO* molecules, $E_{Ru-CO_{n-1}}$ is the energy of the Ru surface with $n - 1$ CO* molecules, and $E_{CO_{(g)}}$ is the energy of one CO(g) molecule. The energies reported in Figure 1 correspond to removing a single CO* species from the lowest energy configuration of adsorbed CO (CO*) at each fractional coverage. CO adsorption energies (-158 ± 1 kJ mol^{-1}) did not vary within the accuracy of the methods used for these calculations for coverages between 0 and 0.33 ML. Previous DFT simulations[55] as well as infrared[56] and low energy electron diffraction (LEED)[32,52] data are consistent with a preference for atop CO* binding on Ru(0001). These binding energies are similar to previous DFT estimates (-164 kJ mol^{-1})[51] and with CO adsorption energies measured from thermal desorption of isolated CO* species on Ru(0001) surfaces (-160 ± 6 kJ mol^{-1}).[31]

CO adsorption energies became less negative, indicative of weaker binding, at coverages above 0.33 ML, as a result of CO* binding on vicinal Ru atoms and of the concomitant repulsion within increasingly dense CO* adlayers on Ru(0001) surfaces. Our DFT estimates show that CO adsorption on Ru(0001) becomes endothermic ($\Delta E_{CO,ads} > 0$) near 0.9 ML CO*, consistent with the submonolayer CO* saturation coverages measured on Ru(0001),[31] Co(0001),[30] and Fe(110)[57] single crystals. These submonolayer CO* saturation coverages on extended flat surfaces appear to reflect the rigid alignment of CO* adlayers, enforced over macroscopic distances by such extended flat geometries. Rigid adlayer arrangements exacerbate CO*–CO* repulsion and lead to surface restructuring as the sole means to achieve higher coverages;[19,33] such restructuring becomes unnecessary on clusters because of facile lateral adsorbate relaxation and of the existence of low-coordination surface atoms that can form geminal dicarbonyls to accommodate multiple CO* species at one metal atom.[34–36] We extend our adsorption calculations to Ru_{201} clusters in the next section to investigate the effects of binding site coordination on CO binding modes and energies as a function of CO* coverage.

3.2. CO* Coverage Effects on CO Binding Energies on Ru_{201} Clusters.

Previous studies have shown that metal clusters allow lateral adlayer relaxations, which minimize repulsive CO*–CO* interactions even at near-saturation CO* coverages.[4] The fcc cuboctahedral Ru_{201} cluster surface (Figure 2) exposes atoms with four distinct coordination numbers (CN = 6–9), associated with exposed corners, edges, (100) terraces, and (111) terraces, respectively. These distinct sites on Ru_{201} clusters are used here to probe CO* binding on surfaces with atoms in diverse coordination environments as well as to probe the effects of coverage on CO* adlayer structures and energetics.

Figure 3 shows adsorption energies for isolated CO* species on essentially bare surfaces and for CO* species at 1 ML coverages on exposed metal atoms with different coordination number on Ru_{201} cluster surfaces. CO adsorption on bare Ru_{201} surfaces becomes weaker (ΔE_{CO*} changes from -173 to -159 kJ mol^{-1}) as the coordination number of adsorption sites
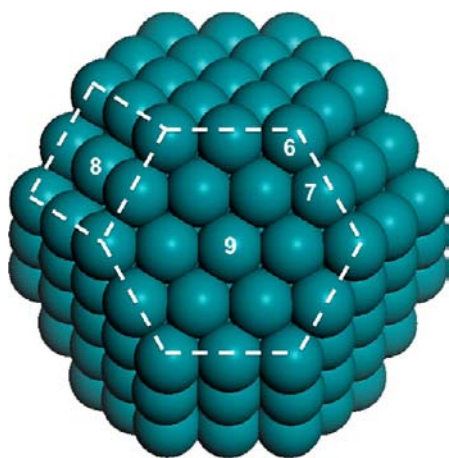
Figure 2. Idealized structural model of the 201-atom cubooctahedral Ru cluster (Ru_{201}) with four distinct surface sites labeled by their nearest-neighbor metal atom coordination number. Dashed lines emphasize the exposed (111) and (100) planes by their hexagonal and cubic symmetry, respectively.
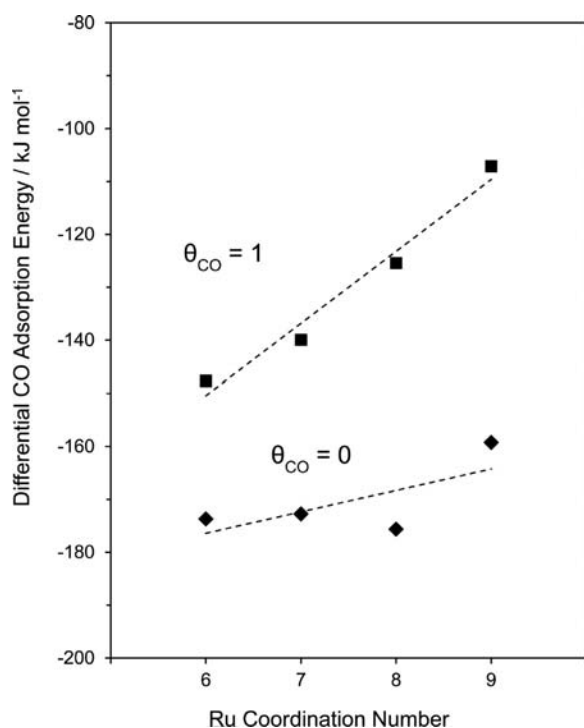

Figure 3. Site coordination number effects on calculated differential adsorption energies for isolated CO* species (◆) and CO* species at one monolayer (CO*/Ru_s, or $\theta_{CO} = 1$) coverage (■) on Ru_{201} clusters.

increases from six at corner sites to nine at (111) terraces; CO adsorption energies also become less negative (−148 to −107 kJ mol^{-1}) as the coordination number of the adsorption site increases at 1 ML CO* coverages (Figure 3) on Ru_{201} clusters. The weakening of M−CO bonds with increasing coordination number of the adsorption site was also observed in DFT studies of CO chemisorption on Pt[4] and Au clusters.[58] These changes in M−CO bond strengths with changes in the coordination number of the adsorption site can be understood in terms of frontier orbital and electron population analyses that examine electron donation from CO* species to the metal and the back

donation of electron density from the metal to CO* species.[59] The electron density available for chemical bonding decreases as the coordination number of a metal atom increases because highly coordinated metal atoms share more electron density with vicinal atoms than atoms in low-coordination environments. The back donation of electron density from metal atoms into M−CO bonding orbitals strengthens M−CO bonds,[60] making metal atoms in low-coordination environments, with their higher electron density, form stronger M-CO bonds than atoms in high-coordination environments.

CO adsorption on the (111) terraces of Ru_{201} clusters is significantly stronger (−108 kJ mol^{-1}) than on Ru(0001) surfaces (+16 kJ mol^{-1}) at 1 ML CO* coverages. The stronger binding of CO* on metal clusters (relative to extended flat surfaces) at high CO* coverages was previously reported and attributed to lateral adlayer relaxation and stronger M−CO bonding caused by an expansion of the M−M distances in surface and subsurface layers, which shifts the d-band center closer to the Fermi level and enhances back donation.[4] These proposals are consistent with Ru−Ru distances in surface and subsurface layers on CO*-covered Ru_{201} clusters (0.271 to 0.28 nm), which are larger than Ru−Ru spacings in the bulk regions of large crystallites (0.2706 nm). Ru−Ru distances in surface layers increase only slightly (0.0015 nm) on CO*-covered Ru(0001) surfaces compared with bare Ru(0001) surfaces. The edges at the intersections of exposed facets of Ru_{201} clusters also allow CO* species at corner/edge sites to deviate significantly from the surface normal (up to 25°). These deviations increase distances among vicinal CO* species on Ru_{201} clusters, while flat extended Ru(0001) surfaces enforce rigid CO* alignments. Intermolecular CO*−CO* repulsion caused at high CO* coverages is attenuated on Ru_{201} clusters by interruptions caused by edges, loosely interpreted as curvature, and by Ru−Ru distances larger than in extended Ru(0001) surfaces.

The exothermic binding of CO* at all Ru_{201} surface sites at 1 ML CO* coverages, taken together with previous reports of supramonolayer (>1 ML) coverages on Ru/SiO_2,[35,36] prompted us to calculate CO* binding energies on Ru_{201} surfaces at coverages above 1 ML. Figure 4 shows the CO* coverage effects on DFT-derived CO adsorption energies on both Ru(0001) and Ru_{201} surfaces. CO* binding on Ru_{201} surfaces remains exothermic >1 ML; corner and edge atoms are able to adsorb more than one CO molecule and, in doing so, increase their overall coordination to values similar to those of exposed atoms in (111) terraces. Adsorbate coverages >1 ML have also been observed in DFT studies of H* adsorption on supported Pt_{13} nanoclusters, in which supramonolayer H* coverages actually induced reconstruction of the Pt cluster.[61] Figure 5 shows the structure of the CO* adlayer on Ru_{201} surfaces at 1.55 ML; in this structure, geminal dicarbonyl species are present at edge and corner sites with calculated binding energies of −35 to −41 kJ mol^{-1} for the removal of one of the two CO* molecules bound at edge and corner atoms, respectively. A CO* coverage of 1.55 ML on Ru_{201} represents the highest CO* coverage that maintains atop CO* binding at atoms in (111) terraces on Ru_{201} surfaces; CO* coverages >1.55 ML require CO* molecules to share Ru atoms in (111) terraces and lead to Ru−CO−Ru bridging species. Infrared data has shown that bridging CO* represent minority species on Ru crystallites at near-saturation CO* coverages;[12,34] therefore 1.55 ML appears to be the highest attainable coverage on Ru_{201} surfaces that remains consistent with predominant CO*
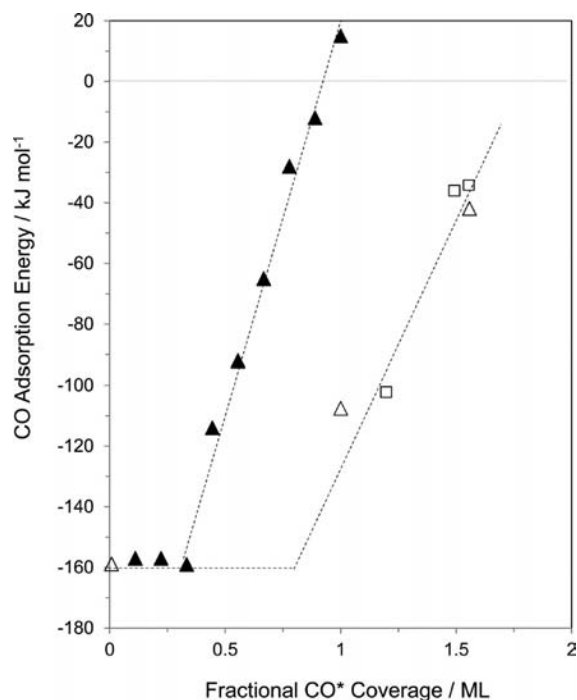
Figure 4. Comparison of CO* coverage effects on CO adsorption energies on the flat, extended 3×3 Ru(0001) surface (filled symbols) and the cubooctahedral Ru_{201} nanocluster (open symbols). Adsorption energies are reported for corner sites ($\square$) for 1 ML < θ_{CO} < 1.55 ML on Ru_{201} because they form geminal dicarbonyl species in this CO* coverage range before subsequent filling of (111) terraces at θ_{CO} > 1.5. All other reported adsorption energies are for terrace sites on Ru(0001) ($\blacktriangle$) and Ru_{201} ($\triangle$).
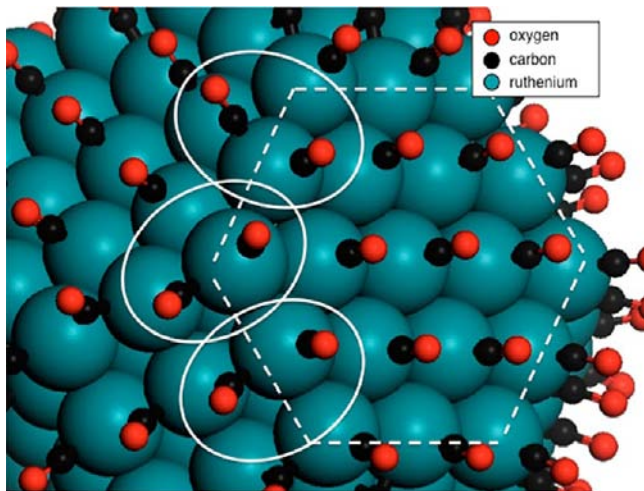

Figure 5. DFT-calculated structures of geminal CO* species (highlighted with ovals) formed at low-coordination corner and edge sites of Ru_{201} (CO* fractional coverage = 1.55 ML). Under-coordinated Ru atoms bind multiple CO species in order to increase their coordination to resemble Ru atoms in close-packed (111) terraces (enclosed by dashed line). (Carbon = black, oxygen = red, ruthenium = teal).

binding in atop positions at high-coordination Ru atoms in terrace environments.

Previous kinetic studies of FTS at near CO*-saturation coverages on Fe, Co, and Ru have reported rate expressions consistent with quasi-equilibrated CO adsorption–desorption

processes.[8−11] CO adsorption–desorption is considered quasi-equilibrated when the adsorption and desorption rates are significantly larger than the net rates of FTS reactions: FTS turnover rates are $(10-40) \times 10^{-3}$ s^{-1} on supported Ru/SiO$_2$ catalysts, at conditions of significant chain growth (H$_2$/CO = 1.5–4, 463–480 K, 560–4000 kPa).[11,28] The rate of CO* desorption from the catalyst surface is given by eq 2:

$$r_{des} = k_{des}(CO^*) = A_{des} \, \exp\left(\frac{-E_{des}}{RT}\right)(CO^*) \tag{2}$$

where r_{des} is the CO* desorption rate, k_{des} is the desorption rate constant, (CO*) is the fractional CO coverage on the catalyst surface, A_{des} is the pre-exponential factor for desorption, E_{des} is the desorption activation energy, R is the gas constant, and T is the temperature. Typical pre-exponential factors are on the order of 10^{13} s^{-1} as a result of the large entropy gains associated with detachment of an adsorbed molecule from a surface into the gas phase.[62] CO* desorption activation energies are essentially the same as the adsorption enthalpy (with opposite sign), because molecular adsorption processes are typically nonactivated. Submonolayer CO* coverages on Ru_{201} surfaces lead to strong CO* binding ($E_{des} \sim 160$ kJ mol^{-1}; Figure 4) that results in desorption rates of ~10^{-5} s^{-1} in the 463–483 K temperature range. These desorption rates on Ru_{201} surfaces at submonolayer CO* coverages are smaller than FTS rates and contradict the assumption of quasi-equilibrated CO adsorption–desorption during FTS reactions.[8−11] CO* desorption energies at 1 ML CO* coverage on Ru_{201} clusters (E_{des} = 104 kJ mol^{-1}; Figure 4) give desorption rates (~ 10 s^{-1}) consistent with CO adsorption–desorption equilibrium, but infrared spectroscopy on supported Ru catalysts detects supramonolayer coverages at CO* saturation.[35] Electron paramagnetic resonance (EPR) spectroscopy later confirmed that Ru carbonyl species existed on CO*-saturated Ru clusters,[36] consistent with supramonolayer CO* coverages. Supramonolayer (1.55 ML) CO* coverages lead to even smaller desorption barriers (42 kJ mol^{-1}; Figure 4) on (111) terraces of Ru_{201} and to even faster CO* desorption rates (2.7×10^8 s^{-1}), also consistent with quasi-equilibrated CO adsorption–desorption during FTS reactions.

The CO* adlayer on Ru_{201} clusters at 1.55 ML CO* coverages contains geminal carbonyl species at low-coordination corner and edge sites. These CO* coverages contain CO* species bound much more weakly than CO* species at lower CO* coverages on these Ru_{201} surfaces. Previous studies have identified $Ru(CO)_x$ (x = 2−3) species using infrared[34,35,63,64] and EPR[36] spectra of CO* species adsorbed on supported Ru catalysts. In the next section, we use infrared spectroscopy to probe CO* species adsorbed on Ru/SiO$_2$ at near-saturation CO* coverages. DFT vibrational analysis was not performed on nearly CO*-saturated Ru_{201} surfaces due to the large (500+ atoms) system size, but high-frequency (>2100 cm^{-1}) vibrations observed in infrared spectra are consistent with the strong C–O bonds associated with geminal Ru carbonyl species,[34,59,60] which our DFT simulations show to be present at corner and edge atoms on Ru_{201} surfaces at near-saturation coverages.

3.3. Infrared Spectra of CO* on Ru/SiO$_2$ at Saturation CO* Coverages. The infrared spectra in Figure 6 show four absorption bands in the C–O stretching region (1700–2250 cm^{-1}) on a Ru/SiO$_2$ catalyst exposed to 0.75 kPa CO at 313 K. H$_2$, O$_2$, and CO chemisorption data showed that the fractional
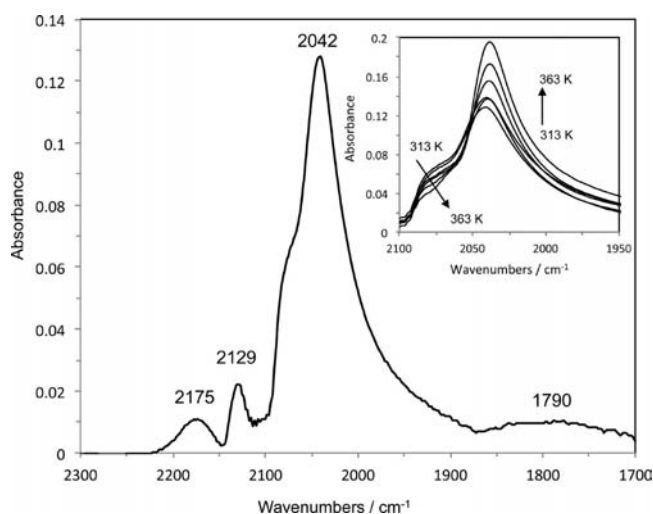
Figure 6. Infrared spectra of a CO*-saturated Ru/SiO$_2$ catalyst (7 nm Ru particles, 0.75 kPa CO, 313 K). CO* saturation was accompanied by no observable changes in the IR spectra with increases in CO pressure. Inset: Intensity increase and band sharpening of the 2042 cm^{-1} absorption band as a function of temperature (0.75 kPa, 313–363 K).

Ru dispersion for this Ru/SiO$_2$ catalyst was 0.12–0.14, which leads to a mean particle size of ~7 nm.[65] No changes in spectral features or intensities were detected as CO pressure increased from 0.2 to 0.75 kPa, indicating the presence of saturated CO* adlayers even at these low pressures. Isothermal CO adsorption spectra at 313 K did not change with time, but an increase in temperature from 313 to 363 K in the presence of 0.75 kPa CO decreased the intensity of the weak band at 2070 cm^{-1} and strengthened, sharpened, and slightly shifted the most intense band (2042–2035 cm^{-1}; Figure 6, inset). The strengthening of the 2042 cm^{-1} band is consistent with higher CO* coverages at 363 K than at 313 K; the narrowing of the 2042 cm^{-1} band is consistent with a more effective dipole alignment of CO* species[4] caused by the annealing of the CO* adlayer into more densely packed and stable structures at 363 K than at 313 K. Subsequent cooling to 313 K did not lead to detectable changes to the spectrum measured at 363 K. The increasing intensity of the 2042 cm^{-1} band with increasing temperature (313–363 K) is unexpected for an exothermic adsorption process based on thermodynamic arguments. Also, isothermal CO adsorption spectra at 313 K did not change with time, leading us to conclude that CO exposure to Ru/SiO$_2$ at 313 K forms a metastable adlayer that is kinetically trapped at these lower temperatures. Significant weakening of CO* binding at near-saturation CO* coverages, consistent with our DFT results for both Ru(0001) and Ru$_{201}$ surfaces, apparently allows the mobility required to restructure and densify CO* adlayers at temperatures slightly above ambient.

CO adlayer densification has also been detected on CO-covered Pt clusters during CO oxidation at 383 K; in this case, CO* bands became more intense during an initial induction period in which surfaces approached steady-state CO* coverages and turnover rates decreased to constant values.[66] FTS turnover rates also decrease with time and then reach constant values.[67–69] These transients appear to reflect surfaces that become less reactive as CO* species form a more stable adlayer; more stable CO* adlayers lead to stronger M–CO bonds and, as a result, less reactive CO* species.

Figure 6 shows bands at 2175, 2129, 2042, and 1790 cm^{-1} (313 K, 0.75 kPa CO) in the C–O stretching region of the infrared spectrum. The band at the highest frequency disappeared when the CO-containing gas stream was replaced with pure He, suggesting that it arises from weakly bound CO* species at frequencies shifted slightly from those for CO(g) (2143 cm^{-1}). The most intense band (2042 cm^{-1} in Figure 6) has been previously assigned to linear CO* bound atop Ru atoms in the high-coordination environment of Ru(0001) surfaces[52] and to similar atop species on supported Ru clusters.[34,59,60] Atoms at high-coordination terraces represent 73% of all exposed atoms in 7 nm fcc cubooctahedra,[17] which is the most stable structure for Ru clusters with >140 atoms.[43] Corner and edge sites in low-coordination environments account for only 9% of all surface atoms in such cubooctahedra, while atoms in (100) terraces account for the other 18%. Figure 6 shows that the 2042 cm^{-1} band is the most dominant feature in the CO* adsorption spectrum (313–363 K, 0.75 kPa CO) and is consistent with the majority of CO* species forming linear Ru–CO complexes on Ru atoms in high-coordination environments, which account for most of the exposed surface atoms for 7 nm Ru cubooctahedra. The weak broad shoulder at 1790 cm^{-1} (Figure 6) lies within the range of bridge-bound CO* species interacting with vicinal Ru atoms,[34] and bridging CO* species exist as minority species only at very high CO* coverages, which cause repulsive CO*–CO* interactions that displace adsorbed CO species from their preferred atop binding sites.[31,52]

The infrared band at 2129 cm^{-1} (Figure 6) reflects the presence of CO* species with stronger C–O bonds than in linear Ru–CO species (2042 cm^{-1}). The C–O stretching frequency for gas-phase CO is 2143 cm^{-1} and decreases as CO binds to metal atoms to form linear Ru–CO species (2042 cm^{-1}). These lower frequencies reflect increasing back donation of electron density from filled metal d-orbitals into the antibonding $2\pi^*$ orbital of CO, which leads to weakening and elongation of C–O bonds and strengthening and contraction of M-C bonds.[70] The 2129 cm^{-1} band, therefore, represents CO* species with stronger C–O bonds (and presumably weaker binding) than linear CO* species in high-coordination environments (2042 cm^{-1}). Metal electron back donation (π-bonding interaction) is not the only descriptor of metal–CO bonding, and X-ray emission spectroscopy has shown that σ (repulsive) and π (attractive) bonding contributions compensate one another during CO binding on Ni surfaces.[55] Such compensation effects preclude definitive inferences about the relations between M–C and C–O bond strengths from C–O vibrational spectra without additional theoretical evidence. Our simulations show stable geminal CO* species at low-coordination Ru sites for CO* coverages near saturation (1.55 ML); such species are bound slightly more weakly (by 5–10 kJ mol^{-1}) than linear atop CO* species. Others have observed infrared bands in the 2070–2150 cm^{-1} range for CO adsorbed on Ru surfaces and assigned them to geminal dicarbonyl and tricarbonyl species (Ru(CO)$_x$, x = 2 or 3) on low-coordination Ru surface atoms[34,59] because of similar frequencies observed for halogenated Ru$_2$CO$_6$ complexes. A Raman band at 2127 cm^{-1} has been reported for axial CO ligands in Ru$_3$(CO)$_{12}$ crystals,[71] for which each Ru atom interacts with four CO ligands; the reported CO* infrared bands at high frequencies (>2040 cm^{-1}) lie within in the range of C–O vibrations in known Ru carbonyls.

Small metal clusters expose a higher fraction of low-coordination atoms than larger metal clusters,[17] and infrared bands for Ru carbonyls, if such species are indeed located preferentially at low-coordination Ru atoms, should become less intense (relative to atop CO* bands) with increasing Ru cluster size. A previous infrared study of CO adsorbed on supported Ru clusters of different size[34] reported a low-frequency band (2028−2050 cm^{-1}) on all Ru clusters, but higher frequency bands (2070−2148 cm^{-1}) were detectable only on Ru clusters <6 nm. These latter bands were assigned to geminal CO* species at low-coordination Ru sites, while the bands at 2028−2050 cm^{-1} were attributed to CO* at high-coordination binding sites.[34] The 2129 cm^{-1} band in the infrared spectra of Figure 6 is in the range of the high frequency (2070−2148 cm^{-1}) bands associated with geminal Ru carbonyl species. These infrared data, taken together with the DFT-derived CO* adlayer structures (Figure 5), are consistent with the presence of geminal CO* species at low-coordination atoms on CO*-covered Ru cluster surfaces.

Our DFT simulations of CO* adsorption on Ru$_{201}$ surfaces show that CO* coverages >1 ML are stable and evolve into more densely covered surfaces via the formation of geminal CO* species; these latter species reside at low-coordination corner and edge sites, consistent with the appearance of high frequency bands (2129 cm^{-1}, Figure 6) on nearly CO*-saturated Ru/SiO$_2$ samples. Geminal CO* species at such low-coordination sites were also detected on Rh[72−74] and Ir[70] clusters and appear to be general features of CO chemisorption on transition metals, which form stable carbonyl complexes as organometallic moieties. The binding of more than one CO* increases the overall coordination number of corner (CN = 6) and edge (CN = 7) atoms to values similar to those for atoms in high-coordination, close-packed surfaces (CN = 9). The tendency of surface metal atoms to maximize their coordination is reminiscent of bond-order conservation principles and of 18-electron configurations of stable organometallic complexes.[66] Repulsive adsorbate−adsorbate interactions become important, and available metal electron density becomes scarce, at the supramonolayer CO* coverages introduced by geminal CO* species at low-coordination Ru sites; these repulsive interactions and depleted electron densities weaken CO* binding (Figure 4), giving rise to metastable adlayers that reconstruct and densify at low temperatures (303 K) without requiring reconstruction of the underlying surface (Figure 6, inset).

Next, we explore CO activation processes on Ru$_{201}$ surfaces at near-saturation CO* coverages; on such surfaces, weak CO* binding allows quasi-equilibrated CO adsorption processes.[8−11] The energetics of elementary steps in CO activation processes are reported here using DFT methods for catalyst surfaces at near CO*-saturation, where CO* coverages strongly influence the binding and reactivity of adsorbed intermediates, for the first time.

3.4. CO* Coverage Effects on FTS Activation Energies.
Eq 3 accurately describes FTS rates on Ru catalysts:[8,11]

$$r_{CO} = \frac{\gamma P_{H_2} P_{CO}}{(1 + \sigma P_{CO})^2} \quad (3)$$

Here, r_{CO} is the CO consumption rate, P_{H_2} and P_{CO} are the H$_2$ and CO pressures, respectively, and γ and σ are kinetic parameters. A set of elementary reaction steps consistent with this equation is required to assign chemical meaning to its kinetic parameters and to define the relevant DFT simulations

required for comparison with measured activation energies. We first introduce the elementary steps for H-assisted CO activation paths consistent with eq 3 and proposed previously on Fe and Co surfaces.[9]

Scheme 1 depicts a sequence of elementary steps for H-assisted CO* activation paths. These steps are consistent with

Scheme 1. Elementary Steps and Their Associated Thermodynamic (K_n) and Kinetic (k_n) Constants for H*-Assisted CO* Activation on Ru Surfaces^a
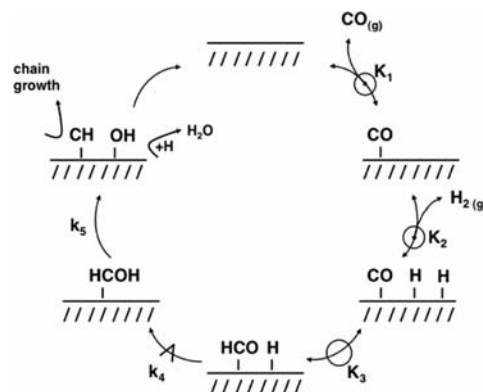
^{a}Quasi-equilibrated steps are denoted by reaction arrows overlaid with a circle, and the kinetically-relevant step is denoted with a reaction arrow overlaid with a carrot symbol.

eq 3 when CO adsorption, H$_2$ dissociation, and CO* hydrogenation to HCO* (Scheme 1, steps 1−3) are quasi-equilibrated, HCO* hydrogenation (Scheme 1, step 4) is irreversible, and CO* is the most abundant surface intermediate (MASI). Quasi-equilibrated CO* dissociation on a vacant surface atom and C* hydrogenation, followed by irreversible CH* hydrogenation would also lead to the form of eq 3 but would require fast and equilibrated CO dissociation and C*−O* recombination. *In-situ* infrared spectra[12] and transient isotopic studies[13] have shown that FTS reactions occur on surfaces nearly saturated with CO*, consistent with the assumption of CO* being the MASI. CO binds very strongly on bare Ru$_{201}$ surfaces (−160 kJ mol^{-1}; Figure 4), making it unlikely that CO* will desorb from the catalyst surface in the time scale of a catalytic turnover. CO adsorption/desorption equilibrium, as a result, is not likely to be achieved on bare Ru$_{201}$ surfaces. We have shown here, however, that CO binds much more weakly (−42 kJ mol^{-1}) on Ru$_{201}$ surfaces near CO*-saturation than on bare Ru$_{201}$ surfaces (−160 kJ mol^{-1}); these near CO*-saturation coverages weaken CO* binding and result in desorption activation barriers that are consistent with quasi-equilibration of CO adsorption−desorption as required by the form of eq 3.

The pseudo-steady-state approximation for all reactive intermediates in Scheme 1, taken together with the assumptions about the quasi-equilibrium of steps 1−3 and CO* as the MASI gives eq 4:

$$r_{CO} = \frac{K_1 K_2 K_3 k_4 P_{CO}}{(1 + K_1 P_{CO})^2} \quad (4)$$

This equation shares the functional form of eq 3 but assigns chemical meanings to the rate parameters ($\gamma = K_1 K_2 K_3 k_4$; $\sigma = K_1$). For CO*-saturated surfaces ($K_1 P_{CO} \gg 1$), eq 4 becomes

$$r_{CO} = \frac{K_2 K_3 k_4 P_{H_2}}{K_1 P_{CO}} = \delta \frac{P_{H_2}}{P_{CO}} \qquad (5)$$

in which δ is a lumped $(K_2 K_3 k_4 K_1^{-1})$ rate constant, with an Arrhenius form:

$$\delta = A \, \exp\left(\frac{-\Delta E_{app}}{RT}\right)$$

$$= A \, \exp\left(\frac{-(\Delta H_2 + \Delta H_3 + \Delta E_4 - \Delta H_1)}{RT}\right) \qquad (6)$$

in which A is the pre-exponential factor, ΔE_{app} is the apparent activation energy, ΔH_n is the enthalpy change for the nth elementary step n in Scheme 1, and ΔE_4 is the activation barrier for the H-assisted CO* dissociation step (step 4).

On these surfaces with saturated CO* adlayers ($K_1 P_{CO} \gg 1$), apparent activation energies (ΔE_{app}) depend on $-\Delta H_1$, the energy required to form a vacancy by desorbing one CO* molecule (eq 6), which depends strongly on CO* coverage (Figure 4), making these activation energies also quite sensitive to CO* coverage. We have chosen a CO* coverage of 1.55 ML on Ru$_{201}$ clusters (with geminal carbonyl species at low-coordination sites and CO* species that can maintain equilibrium with the contacting CO(g)) as a reasonable representation of Ru cluster surfaces at near-saturation CO* coverages during FTS reactions.

The precise CO* coverages during FTS reactions remain experimentally inaccessible. Surfaces exhibit complex inter-actions within the adlayer at high CO* coverages, including intermolecular repulsion and dipole coupling.[4,75,76] These interactions are nonadditive and thus difficult to determine using current DFT methods. Rigorous determination of the CO* coverage that corresponds to near-CO* saturation, which would require *ab initio*-based kinetic simulations of CO adsorption, desorption, and surface diffusion as well as the incorporation of all lateral CO*−CO* interactions within the adlayer, is beyond the scope of this work.

These Ru$_{201}$ clusters with 1.55 ML CO* coverages are used next to obtain DFT-derived energies of reactants, products, and transition states for the elementary steps in the H-assisted CO activation path (Scheme 1), which is consistent with all rate data on Fe, Co, and Ru catalysts.[8−11] These DFT-derived apparent activation energies are compared with those for routes involving CO* dissociation on a vicinal vacant Ru atom on both (111) terraces and low-coordination corner and step-edge atoms in these Ru clusters. Previous DFT studies have suggested that direct CO dissociation becomes facile when carried out on vacant metal atoms in low-coordination environments and low CO* coverages.[18,21−23] This present study compares for the first time DFT-derived barriers for H-assisted paths on (111) terraces to direct paths on metal atoms with different coordination on Ru clusters at relevant near CO*-saturation coverages.

3.5. Contributions from Hydrogen-Assisted and Direct CO Dissociation Paths in CO Hydrogenation on CO*-Covered Ru Cluster Surfaces. H*-assisted CO activation routes (Scheme 1) are consistent with the measured effects of H$_2$ and CO on FTS rates and on oxygen removal selectivities for Co- and Fe-based catalysts and also with DFT estimates of activation energies at 0.5 ML CO* coverages on extended, low-index Fe and Co surfaces.[9] These previous studies are extended here to Ru$_{201}$ clusters saturated with CO*

in order to reflect the size, shape, and CO* coverages in working FTS catalysts. In doing so, we examine more rigorously the relative contributions of H-assisted and direct CO dissociation paths on relevant surfaces at saturation CO* coverages.

The H-assisted CO activation path (Scheme 1) involves the quasi-equilibrated steps of molecular CO adsorption, H$_2$ dissociation, and CO* hydrogenation to formyl (HCO*), followed by irreversible reactions of HCO* and H* to form hydroxymethylene (HCOH*). At near CO* saturation cover-ages, such elementary steps lead to an apparent activation energy that reflects the enthalpy of quasi-equilibrated steps and the barrier for the kinetically relevant step (eq 6). H-assisted CO* activation can also occur by H-addition to the O-atom in CO* to form hydroxy-carbonyls (COH*) that add a H-atom to form hydroxymethylene, which dissociates into CH* and OH*.

Table 1 shows the activation barriers and reaction enthalpies for these steps and Figure 7 shows the DFT-derived reaction

Table 1. Calculated Activation Energies and Reaction Enthalpies for Reactions of CO* with H* and for Reactions of HCO* with H* and * (Vacant Surface Metal Site) on the (111) Terrace of Ru$_{201}$ (1.55 ML CO*)

step	E_{act}, kJ mol^{-1}	ΔH_{rxn}, kJ mol^{-1}
CO* + H* → HCO* + *	81	50
CO* + H* → COH* + *	167	−11
HCO* + * → CH* + O*	155	−84
HCO* + H* → HCOH* + *	88	16

coordinate for formyl-mediated CO activation (Scheme 1). A vacancy forms via CO desorption ($-\Delta H_1 = 42$ kJ mol^{-1}), H* forms via H$_2$ dissociation ($\Delta H_2 = -15$ kJ mol^{-1}), and H* reacts with a vicinal CO*. Figures 8 and 9 show DFT-derived reactant, transition state, and product structures for HCO* and
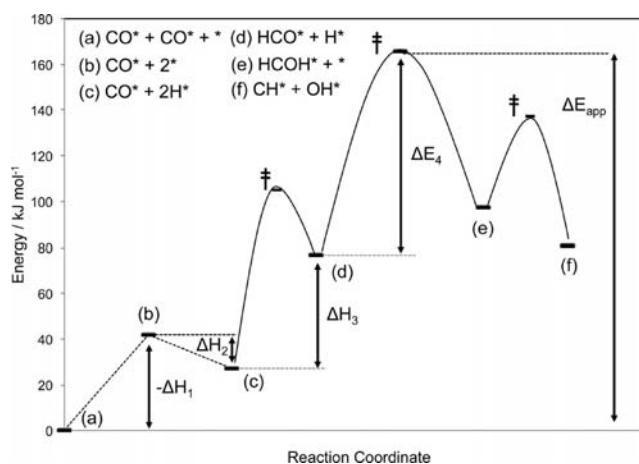

Figure 7. DFT-calculated energy diagram for the elementary steps (Scheme 1) involved in the H-assisted CO* activation path on the (111) terrace of Ru$_{201}$ (1.55 ML CO*). The apparent activation energy for the H*-assisted path is a sum of the energy required to generate a vacancy ($-\Delta H_1$) from a CO*-covered surface (a), the enthalpy of H$_2$ adsorption (ΔH_2; (b) to (c)), the enthalpy of H* addition to CO* (ΔH_3; (c) to (d)), and the activation barrier for H* addition to HCO* (ΔE_4, (d) to (e)). The barrier for the dissociation reaction of HCOH* to CH* + OH* ((e) to (f)) is shown to justify the irreversibility of HCO* hydrogenation. Transition-state energies are denoted by double daggers.
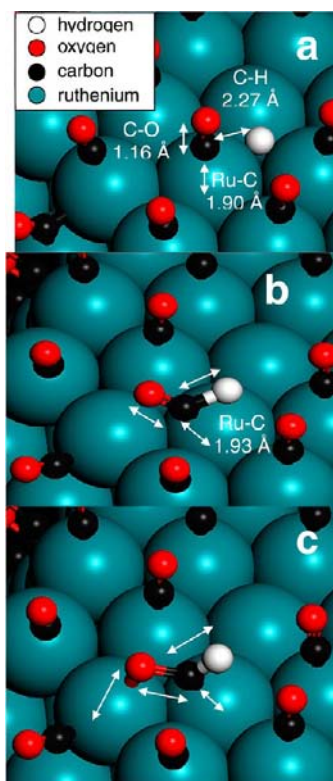
Figure 8. DFT-calculated reactant (a), transition (b), and product (c) states for quasi-equilibrated H* addition to CO* to form formyl (HCO*) on (111) terraces of Ru_{201} at 1.55 ML CO* coverage. Refer to Scheme 1 for the complete set of elementary steps for the H*-assisted path. (Hydrogen = white, carbon = black, oxygen = red, ruthenium = teal).

Figure 9. DFT-calculated reactant (a), transition (b), and product (c) states for irreversible H* addition to HCO* to form hydroxymethylene (HCOH*) on (111) terraces of Ru_{201} at 1.55 ML CO* coverage. The reader is referred to Scheme 1 for the complete set of elementary steps for the H*-assisted path. (Hydrogen = white, carbon = black, oxygen = red, ruthenium = teal).

HCOH* formation, respectively, on Ru_{201} (111) terraces at 1.55 ML CO* coverages. On these surfaces, H* inserts into a Ru—CO bond to form a three-center H*—Ru—CO* transition state (Figure 8b) that mediates formyl formation ($\Delta H_3 = 50$ kJ mol^{-1}). Both transition and product states are stabilized by the formation of η^2 di-σ bound Ru—C(H)—O—Ru species, which forms via concerted CO* migration from the vicinal Ru site (Ru_2) on CO*-covered surfaces to allow CO* to interact with a vacant site. Such concerted migrations are ubiquitous on relevant crowded surfaces but pose formidable challenges for theory and require costly *ab initio* molecular dynamics simulations for a wide range of adsorbate configurations to account for concerted motions over extended distances. CO* migrations on CO*-crowded surfaces can cause activation energies to vary by as much as 20 kJ mol^{-1}.

The calculated activation barrier for direct dissociation of HCO* to CH* and O* (155 kJ mol^{-1}) was more than 67 kJ mol^{-1} higher than for HCO* hydrogenation to hydroxymethylene (HCOH*) (88 kJ mol^{-1}), suggesting that HCOH* formation is the preferred route toward C—O bond cleavage in H-assisted CO* activation paths. CO* and H* can react to form COH* (instead of HCO*) but with an activation barrier (167 kJ mol^{-1}) much higher than for HCO* formation (81 kJ mol^{-1}), indicating that H-addition at the C-atom in CO* is the preferred hydrogenation route. The high barriers for HCO* decomposition and for COH* formation suggest that H-addition to HCO* is the sole kinetically relevant step in CO* activation, and we consider only the formation and
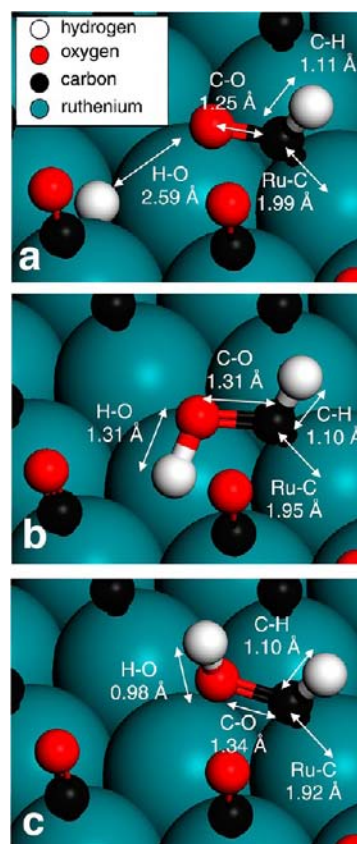
decomposition of hydroxymethylene (HCOH*) species in our following analyses.

HCOH* forms as HCO* reacts with H* (Figure 9) with a barrier (ΔE_4) of 88 kJ mol^{-1}. Figure 7 shows that the DFT-derived activation energy for H-assisted CO activation on (111) terraces of Ru_{201} clusters at 1.55 ML CO* coverages is 165 kJ mol^{-1}. These values are much smaller than those for the unassisted (direct) CO dissociation (322 kJ mol^{-1}), a route that we examine in more detail below. The overall H-assisted barriers (165 kJ mol^{-1}) also resemble measured FTS activation barriers (90—120 kJ mol^{-1}) on Ru catalysts[11,28] more closely than those for the direct path. The DFT-derived activation energy for the H-assisted path suggests that CO can be activated with the assistance of H* atoms on low-index planes. Direct CO activation paths, which in any case cannot account for the measured effects of reactant pressures on FTS rates and oxygen removal selectivities, are in fact unnecessary for CO* activation at the near CO*-saturation coverages that prevail during FTS reactions.

The rate equation for the H-assisted CO activation path is predicated on the assumptions that CO and H_2 adsorption as well as CO* hydrogenation (to HCO*) are quasi-equilibrated. H_2—D_2 isotope scrambling occurs rapidly in H_2/D_2/CO reactant streams on supported Ru^{77} and Co^{78} catalysts, suggesting that H_2 and D_2 adsorb dissociatively and recombine much faster that forward reactions of H* that lead to CO and H_2 consumption during FTS. The calculated activation energy

for H_2 dissociation (31 kJ mol^{-1}) and for its reverse reaction (2H* recombination, 57 kJ mol^{-1}) on CO*-saturated (111) terraces of Ru$_{201}$ clusters is much smaller than that for H-assisted CO* activation (165 kJ mol^{-1}), also indicating that H_2 adsorption is quasi-equilibrated at saturation CO* coverages relevant to FTS. Such rapid adsorption/desorption processes ensure that H* species, irrespective of their activation mechanism, are available without kinetic restraint to react with vicinal adsorbed species (CO*) in the time scale of a catalytic turnover. The reversibility of CO* hydrogenation to HCO* can be inferred from the forward rate of HCO* hydrogenation (step 4; Scheme 1) relative to that of HCO* decomposition to CO* and H* (reverse of step 3; Scheme 1). HCO* formation is considered to be in quasi-equilibrium when its reverse (HCO* decomposition) occurs much faster than its forward reaction (HCO* hydrogenation). Both HCO* hydrogenation and HCO* decomposition are surface-catalyzed reactions and, as a result, are likely to have similar pre-exponential factors; therefore, activation barriers for HCO* hydrogenation and HCO* decomposition determine their relative rates. Our DFT calculations show that HCO* decomposition barriers (31 kJ mol^{-1}; Figure 7) are much smaller than HCO* hydrogenation barriers (88 kJ mol^{-1}, Figure 7); therefore, we conclude that HCO* decomposition occurs much faster than HCO* hydrogenation, consistent with quasi-equilibrated formation of HCO* intermediates.

The form of eq 4 requires HCO* hydrogenation (step 4; Scheme 1) to be the first irreversible step in the H-assisted CO activation mechanism. The irreversible nature of HCO* hydrogenation to HCOH* is determined by the relative rates of its reverse reaction (HCOH* decomposition to HCO* and H*) and of HCOH* decomposition to CH* and OH* (step 5, Scheme 1). Both forward and reverse HCOH* reactions are unimolecular and expected to have similar pre-exponential factors. Figure 7 shows that the calculated barrier for HCOH* decomposition to HCO* and H* is 21 kJ mol^{-1} larger than for HCOH* decomposition to CH* and OH*. This barrier difference makes HCOH* decomposition to CH* and OH* faster than HCOH* decomposition to HCO* and H* and the step that forms HCOH* formation (step 4, Scheme 1) essentially irreversible. The DFT-derived energies of the intermediates and transition states in the H-assisted CO activation path (Scheme 1) are consistent with the quasi-equilibrium assumptions for steps 1−3 and with the kinetic relevance of step 4.

Next, we explore proposals about the relevance of direct CO* dissociation paths and the requirements for special surface sites with low coordination to catalyze such reactions during FTS. CO* activation during FTS may also occur via CO* dissociation on vicinal vacant sites.[12,18,73,79,80] Scheme 2 shows a sequence of elementary steps for such paths in which each step is reversible; we comment later on the kinetic relevance of each step after presenting our DFT-derived energy profile for the direct paths.

Unassisted CO* activation paths involve C−O bond dissociation on a vicinal vacant Ru atom. Figure 10 shows the reactant, transition, and product state structures for direct CO* dissociation on (111) terraces of Ru$_{201}$ clusters (Scheme 2, step 6) at 1.55 ML CO* coverage. The DFT-derived activation and reaction energies for direct CO* dissociation steps are 280 and 113 kJ mol^{-1}, respectively. The direct path involves the migration of a CO* molecule toward a vacancy and the subsequent tilting of this CO* molecule toward the (111)

Scheme 2. Elementary Steps and Their Associated Kinetic (k_n) Constants for Direct CO* Activation on Ru Surfaces
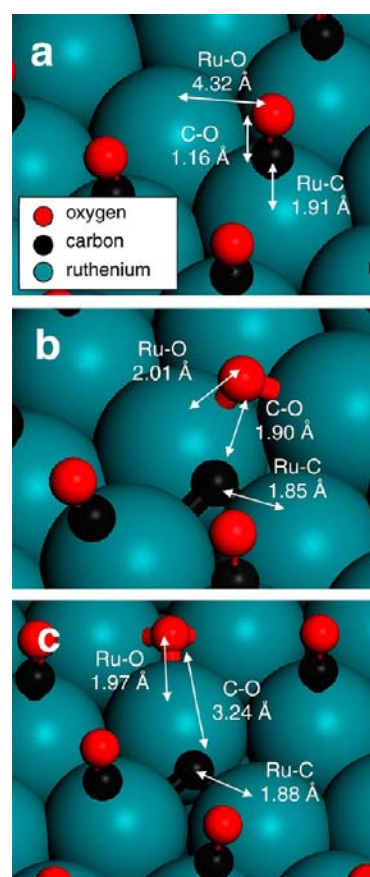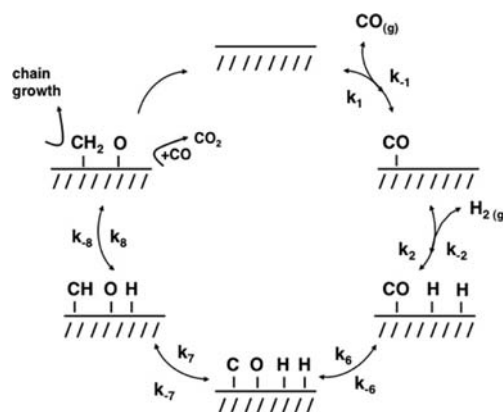

Figure 10. DFT-derived reactant (a), transition (b), and product (c) state structures for direct C−O bond activation (Scheme 2, step 6) on the (111) terraces of Ru$_{201}$ at 1.55 ML CO* coverage. Refer to Scheme 2 for the complete set of elementary steps for the direct path. (Carbon = black, oxygen = red, ruthenium = teal).

terrace of the Ru$_{201}$ surface. The insertion of an exposed Ru atom into the C−O bond activates CO* in the transition state, as shown in Figure 10b. The resulting C* and O* fragments then relax into stable bound species at three-fold hollow sites in the product state (Figure 10c). The direct CO* dissociation reaction is endothermic (+113 kJ mol^{-1}) because of the repulsive interactions from metal atom sharing and the through-space interactions of C* and O* between them and with vicinal CO* species. The intrinsic barrier for this reaction

($\Delta E_6 = 280$ kJ mol^{-1}) is actually larger than that reported for direct CO dissociation on Ru(0001) surfaces (227 kJ mol^{-1}) at low CO* coverages (<0.25 ML).[20] The near-saturation CO* coverages on the Ru$_{201}$ cluster exacerbate the repulsive interactions between the C* and O* species and vicinal CO* species at transition states and lead to higher barriers than those reported on bare Ru(0001) surfaces.

CO* dissociation must be reversible for any direct CO* dissociation path to be consistent with FTS rate equations (eq 3).[8−11] The assumption regarding the reversibility of CO* dissociation (step 3, Scheme 2) can be probed by comparing the reverse barriers of such steps to the forward barriers of C* hydrogenation to CH* (step 4, Scheme 2) on the (111) terraces of CO*-saturated (1.55 ML) Ru$_{201}$ cluster surfaces. The reversal of direct CO* dissociation steps (C* and O* recombination) has a DFT-derived barrier of 164 kJ mol^{-1}; the calculated activation barrier for C* hydrogenation to CH* is 45 kJ mol^{-1}, suggesting that if C* species formed, they would preferentially react with H* (to form CH*) instead of with O* (to form CO). Thus, any direct CO* dissociation steps on (111) terraces on Ru$_{201}$ at 1.55 ML CO* coverages would occur irreversibly (and with large activation energies); these simulations suggest that such steps, ubiquitously proposed as the underlying basis for eq 3 on Co,[81] Fe,[82,83] and Ru[12,73] catalysts, are implausible on the active low-index planes of Ru clusters.

Irreversible CO* dissociation steps, taken along with CO* as the MASI leads to the rate equation:

$$r_{CO}^{direct} = \frac{K_1 k_6 P_{CO}}{(1 + K_1 P_{CO})^2} \tag{7}$$

On surfaces nearly saturated with CO* ($K_1 P_{CO} \gg 1$), eq 7 becomes

$$r_{CO}^{direct} \approx \frac{k_6}{K_1 P_{CO}} = \varepsilon \left(\frac{1}{P_{CO}} \right) \tag{8}$$

in which the effective rate constant ε is given by

$$\varepsilon = A_{direct} \exp \left(\frac{-\Delta E_{app}^{direct}}{RT} \right) = A_{direct} \exp \left(\frac{-(\Delta E_6 - \Delta H_1)}{RT} \right) \tag{9}$$

Here, A_{direct} is the apparent pre-exponential factor for the direct path and ΔE_6 and ΔH_1 are the activation energy and reaction enthalpy of step 6 and step 1 in Scheme 2, respectively.

Figure 11 shows the DFT-derived energy diagram for irreversible, unassisted CO* dissociation on the (111) terraces of Ru$_{201}$ surfaces at 1.55 ML CO*; the apparent activation energy ($-\Delta H_1 + \Delta E_6$) for this path is 322 kJ mol^{-1}. Enthalpies of quasi-equilibrated elementary steps as well as activation energies of the kinetically relevant steps for both the direct and H-assisted CO* activation paths are shown for comparison in Table 2. The apparent activation energy for the direct CO activation path is 157 kJ mol^{-1} larger than H-assisted CO* activation on (111) terraces of Ru$_{201}$ clusters at near-saturation CO* coverages (1.55 ML), making direct CO activation unlikely during FTS on Ru catalysts. The irreversible nature of CO* dissociation and its high activation barrier require that active FTS surfaces use more facile bimolecular CO* activation routes to achieve observed reaction rates. Any sequence of elementary steps involving unassisted CO* dissociation must equilibrate this step and the first H* addition to its C* products
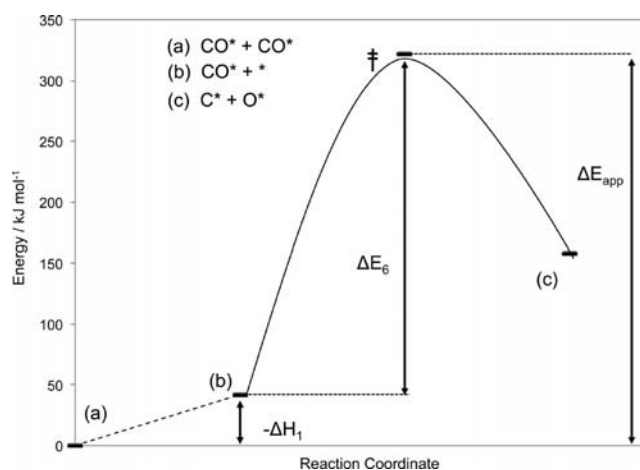

Figure 11. DFT-derived energy diagram for vacancy generation and direct CO* activation on (111) terraces of Ru$_{201}$ (1.55 ML CO*). The apparent activation energy (ΔE_{app}) for the direct path is a sum of the energy required to generate a vacancy ($-\Delta H_1$) from a CO*-covered surface (a) and the intrinsic activation energy (ΔE_6) for direct activation of CO* by a surface vacancy (b) to form chemisorbed C* and O* species (c). See Scheme 2 for a complete description of the elementary steps involved in the direct path. Transition-state energies are denoted by double daggers.

and require that CH* + H* reactions be the first irreversible step for agreement with measured rate equations (eq 3).[8−11] DFT results show that CH* decomposition to C* and H*, the microscopic reverse of C* hydrogenation (Scheme 2; step 7), has a higher barrier (150 kJ mol^{-1}) than CH* hydrogenation to CH$_2$* (40 kJ mol^{-1}), a result that is inconsistent with CH* hydrogenation (Scheme 2; step 8) as the first irreversible step in direct CO* activation paths on nearly CO*-saturated (111) terraces of Ru$_{201}$ clusters. Our DFT-derived reaction energies indicate that CO* dissociation on (111) terraces of CO*-saturated Ru$_{201}$ clusters is irreversible and involves activation energies that render such steps unproductive in FTS reactions. As a result, CO* dissociation must occur with H-assistance.

Previous studies have proposed that direct CO dissociation becomes facile (and perhaps reversible) only on low-coordination step-edge or corner sites, thus avoiding the high CO* dissociation barriers prevalent on high-coordination atoms on Ru,[18,20] Co,[19,21] Rh,[22] and Fe[23] surfaces at low-CO* coverages. These proposals seem to find support in scanning tunneling microscopy (STM) studies that detect roughening of extended Co(0001) surfaces upon exposure to synthesis gas (4 bar, H$_2$/CO = 2523 K) to form monatomic step-edge sites claimed to act as direct CO* dissociation sites in FTS reactions.[19] DFT studies have concluded also that direct CO* dissociation occurs preferentially at step-edge sites.[22] Next, we calculate activation energies for direct CO* dissociation on low-coordination atoms at Ru$_{201}$ cluster surfaces saturated with CO* and compare them to those for direct and H-assisted CO* activation paths on high-coordination atoms at similar CO* coverages.

3.6. CO* Dissociation on Low-Coordination Ru Atoms and Cluster Size Effects on FTS Rates. DFT-derived reactant, transition state, and product structures for direct CO activation on the Ru$_{201}$ corner site are shown in Figure 12. The activation energy ($-\Delta H_1 + \Delta E_6$; eq 9) for direct CO activation on the Ru$_{201}$ corner site is 356 kJ mol^{-1}, which is actually 34 kJ mol^{-1} higher than for the same reaction on the (111) terraces

Table 2. Elementary Steps and Their DFT-Calculated Reaction Enthalpies and Activation Energies for H*-Assisted and Direct CO* Activation Paths on the (111) Terrace of Ru$_{201}$ (1.55 ML CO*)^a

CO Activation Path	Step		Energy (kJ mol^{-1})
H*-assisted	1. CO$_{(g)}$ + * ⇌ CO*	ΔH_1	-42
	2. H$_{2(g)}$ + * ⇌ 2H*	ΔH_2	-15
	3. CO* + H* ⇌ HCO* + *	ΔH_3	50
	4. HCO* + H* ⟶ HCOH* + *	E_4	88
	$E_{app} = \Delta H_2 + \Delta H_3 + E_4 - \Delta H_1$		165

	Step		Energy (kJ mol^{-1})
Direct	1. CO$_{(g)}$ + * ⇌ CO*	ΔH_1	-42
	6. CO* + * ⟶ C* + O*	E_6	280
	$E_{app} = E_6 - \Delta H_1$		322

^{a}Quasi-equilibrated steps are denoted by reaction arrows with a circle, the kinetically-relevant step is denoted with reaction arrows with a carrot symbol, and the vacant surface sites are denoted by *.
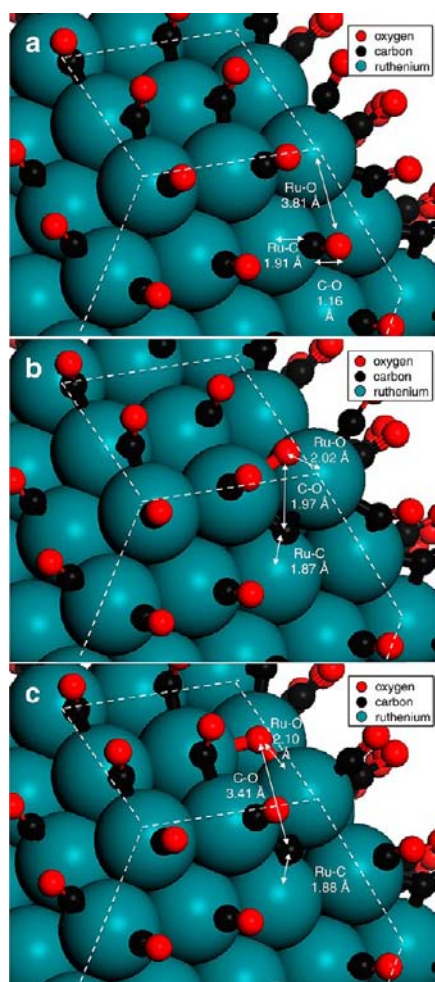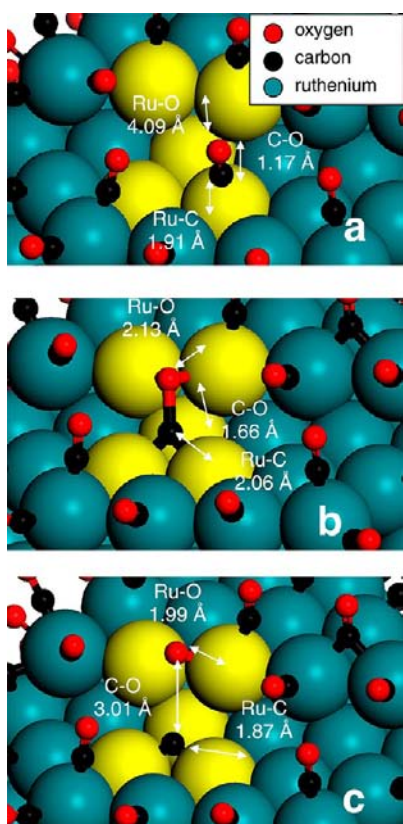

Figure 12. DFT-derived reactant (a), transition (b), and product (c) state structures for direct C−O bond activation (Scheme 2, step 6) on the corner sites of Ru$_{201}$ at 1.55 ML CO* coverage. Refer to Scheme 2 for the complete set of elementary steps for the direct path. (Carbon = black, oxygen = red, ruthenium = teal).

of these clusters at the same CO* coverage (1.55 ML). CO* activation at these corner sites involves a transition state in which the incipiently formed C* and O* species interact repulsively with each other and with the vicinal CO* species residing at the low-coordination corner and edge Ru atoms at 1.55 ML CO* coverages (Figure 12). These repulsive interactions lead to a larger intrinsic barrier for direct C−O dissociation at corner atoms than at atoms in (111) terraces, because CO* species in (111) terraces are packed less densely than geminal CO* carbonyls at corner and edge sites. At these CO* coverages, Ru atoms in low-coordination environments are even less reactive than those in low-index planes for direct C−O bond dissociation, a conclusion that differs markedly from those derived from DFT simulations of CO* dissociation on bare, extended step Ru[18,20] and Co[21] surfaces.

We have used the (111) terraces of Ru$_{201}$ surfaces at near CO*-saturation coverages as a surrogate for the working catalyst during FTS reactions; these (111) terraces feature highly coordinated Ru atoms that account for >75% of surface atoms for Ru clusters >9 nm.[17] CO consumption turnover rates for clusters in this size range are independent of cluster size, and rates are higher than on smaller clusters.[16] FTS turnover rates decrease strongly with decreasing cluster size (clusters <10 nm) on Ru and Co catalysts.[11,14,16] The fraction of surface sites in low-coordination environments increases with decreasing particle size,[17] As a result, the observation that small clusters are less reactive than large clusters is inconsistent with CO activation reactions preferentially occurring on low-coordination corner and edge atoms, irrespective of whether CO activation occurs directly or with H-assistance.

The unreactive nature of corner and edge atoms reflect the requirement for vacant sites at such locations. These vacancies are required for both direct and H-assisted CO activation paths and are unlikely to exist at corner or edge atoms, which tend to maximize their overall coordination number by forming geminal dicarbonyl species (Figure 5 and 2129 cm^{-1} band in Figure 6) at near-saturation CO* coverages. Our DFT-derived activation barriers show that, even in the unlikely event of a vacant Ru corner atom at high CO* coverages, direct CO activation has an effective barrier that is 34 kJ mol^{-1} larger than the activation energy for direct CO activation on vacant Ru atoms in (111) terraces of Ru$_{201}$ clusters. CO dissociation reactions on vacant Ru atoms, irrespective of coordination, must overcome activation barriers that are larger than H-

assisted CO dissociation on (111) terraces by 157 kJ mol^{-1} on vacancies in (111) terraces and by 191 kJ mol^{-1} on corner vacancies. Low-coordination atoms are therefore not required for CO dissociation during FTS reactions. CO* activation on these sites lead to inconsistencies with both measured rate equations and with DFT-derived activation barriers on CO*-saturated Ru cluster surfaces and cannot be supported by either experiment or theory.

Recent theoretical studies[18,22,23] suggest that direct CO* activation occurs preferentially at special B5 step-edge sites (Figure 13) on bare Co,[21] Ru,[18] and Rh[22] surfaces. These sites

Figure 13. DFT-derived reactant (a), transition (b), and product (c) state structures for direct CO* activation (Scheme 2, step 6) on the B5 step-edge site (labeled in yellow) of Ru$_{201}$ at 1.07 ML CO* coverage. Refer to Scheme 2 for the complete set of elementary steps for the direct path. (Carbon = black, oxygen = red, ruthenium = teal).

consist of five metal atoms, two of which are metal atoms (with CN = 7) in the upper (111) terrace at the step-edge (Figure 13). The remaining three metal atoms that compose the B5 site include two atoms at the base of the step-edge (CN = 11) and one remaining metal atom in the exposed lower (111) terrace (CN = 9). The DFT-derived reactant, transition state, and product structures for direct CO activation at the uniquely positioned B5 step-edge sites on Ru$_{194}$ surfaces at 1.07 ML CO* coverages are shown in Figure 13. Such coverages (1.07 ML) were used in order to generate geminal dicarbonyl species on the step-edge analogous to those observed on low-coordination sites on the CO*-saturated Ru$_{201}$ cluster surface (1.55 ML). The intrinsic barrier for direct CO activation at the B5 step-edge site is 150 kJ mol^{-1}, and the CO* adsorption energy (ΔH_1; eq 6), which is required to form a vacant Ru atom on the step-edge site during FTS at saturation coverages,

is -119 kJ mol^{-1}. This leads to an effective activation energy ($-\Delta H_1 + \Delta E_6$) of 269 kJ mol^{-1} for direct CO dissociation at such step-edge sites. The intrinsic direct CO activation barrier (ΔE_6) reported here is larger than barriers reported for CO activation on the low-coordination B5 sites and 4F-bridge sites by 61 and 85 kJ mol^{-1}, respectively, on bare extended Ru surfaces.[18] These high barriers on B5 sites of Ru$_{194}$ surfaces reflect strong repulsive interactions at the required transition states at these high CO* coverages (Figure 13). The effective activation energy for direct CO* dissociation at B5 sites is still 104 kJ mol^{-1} larger than the H-assisted CO* activation path on (111) terraces of CO*-saturated Ru$_{201}$ cluster surfaces. Such special low-coordination sites are unlikely, in any case, to prevail at relative abundances independent of cluster size and seem more likely to exist, in fact, on small clusters where measured turnover rates are much lower than on larger Ru[16] and Co[14] clusters.

Our DFT estimates of apparent activation energies on Ru$_{201}$ cluster surfaces saturated with CO* are consistent with CO* occurring predominantly on low-index planes via H-assisted paths that involve CO* reacting with coadsorbed H* atoms, instead of vicinal vacant Ru sites that are scarce at high CO* coverages. These H-assisted paths have been previously proposed to occur on Co[9,27,84,85] and Fe[9,86] surfaces and are consistent with measured FTS rates and oxygen removal selectivities for FTS on Ru catalysts.[8,11] DFT-derived activation energies have shown that direct CO dissociation on vacant Ru atoms, irrespective of coordination, is essentially irreversible and inconsistent with FTS rate equations. We have also shown that CO adsorption becomes weaker with increasing CO* coverage and that this destabilization of adsorbed CO* species at near-saturation CO* coverages allows the equilibration of CO adsorption−desorption processes during FTS reactions. DFT simulations of chemical reactions on surfaces with relevant adsorbate coverages are necessary because coverages affect adsorbate binding and reactivity. Surface adsorbate coverage can also determine the identity of the kinetically relevant step in heterogeneous catalytic reactions, which makes the use of relevant surface coverages in DFT modeling vital for verifying catalytic mechanisms and predicting catalyst reactivity.

4. CONCLUSIONS

FTS occurs on Ru surfaces near CO*-saturation conditions that can be simulated by CO* coverages above one monolayer on Ru$_{201}$ cluster surfaces. DFT simulations show that supra-monolayer coverages on Ru$_{201}$ cluster surfaces evolve via formation of geminal CO* species, consistent with infrared spectra of CO* at saturation coverages on Ru/SiO$_2$, that exist at low-coordination corner and edge atoms. Surface metal atoms tend to increase their coordination number by interacting with multiple adsorbed species at high coverages instead of by surface reconstruction. CO* coverage affects adsorption energies, heats of reaction, and activation energies that contribute to effective activation barriers for CO* activation paths in FTS reactions. DFT simulations show that CO* is activated predominantly via H-assisted paths on high-coordination Ru atoms in (111) terrace environments on CO*-saturated Ru$_{201}$ cluster surfaces, consistent with measured FTS rate equations, oxygen rejection selectivities, and particle size effects on FTS rates. CO* dissociation is essentially irreversible on both high- and low-coordination Ru atoms and, as a result, inconsistent with measured FTS rate expressions. This study shows that high adsorbate coverages control adsorption

behavior and reactivity of catalyst surfaces. As a result, the use of relevant surface coverages is of paramount importance when using theoretical models to simulate heterogeneous catalytic reactions.

AUTHOR INFORMATION

Corresponding Author
iglesia@berkeley.edu; mn4n@virginia.edu

Notes
The authors declare no competing financial interest.

REFERENCES

(1) Garcia-Dieguez, M.; Chin, Y. H.; Iglesia, E. J. Catal. 2012, 285, 260.

(2) Chin, Y. H.; Buda, C.; Neurock, M.; Iglesia, E. J. Am. Chem. Soc. 2011, 133, 15958.

(3) Chin, Y. H.; Iglesia, E. J. Phys. Chem. C 2011, 115, 17845.

(4) Allian, A. D.; Takanabe, K.; Fujdala, K. L.; Hao, X.; Truex, T. J.; Cai, J.; Buda, C.; Neurock, M.; Iglesia, E. J. Am. Chem. Soc. 2011, 133, 4498.

(5) Langmuir, I. Trans. Faraday Soc. 1922, 17, 621.

(6) Djega-Mariadissou, G.; Boudart, M. J. Catal. 2003, 216, 89.

(7) Berlowitz, P. J.; Peden, C. H. F.; Goodman, D. W. J. Phys. Chem. 1988, 92, 5213.

(8) Dixit, R. S.; Tavlarides, L. L. Ind. Eng. Chem. Process Des. Dev. 1983, 22, 1.

(9) Ojeda, M.; Nabar, R.; Nilekar, A. U.; Ishikawa, A.; Mavrikakis, M.; Iglesia, E. J. Catal. 2010, 272, 187.

(10) Yates, I. C.; Satterfield, C. N. Energy Fuels 1991, 5, 168.

(11) Loveless, B. T.; Iglesia, E. J. Catal. 2013, to be submitted.

(12) Winslow, P.; Bell, A. T. J. Catal. 1984, 86, 158.

(13) Mims, C. A.; McCandlish, L. E. J. Phys. Chem. 1987, 91, 929.

(14) den Breejen, J. P.; Radstake, P. B.; Bezemer, G. L.; Bitter, J. H.; Froseth, V.; Holmen, A.; de Jong, K. P. J. Am. Chem. Soc. 2009, 131, 7197.

(15) Park, J. Y.; Lee, Y. J.; Khanna, P. K.; Jun, K. W.; Bae, J. W.; Kim, Y. H. J. Mol. Catal. A: Chem. 2010, 232, 84.

(16) Carballo, J. M. G.; Yang, J.; Holmen, A.; Garcia-Rodriguez, S.; Rojas, S.; Ojeda, M.; Fierro, J. L. G. J. Catal. 2011, 284, 102.

(17) van Hardeveld, R.; Hartog, F. Surf. Sci. 1969, 15, 189.

(18) Shetty, S.; Jansen, A. P. J.; van Santen, R. A. J. Am. Chem. Soc. 2009, 131, 12874.

(19) Shetty, S.; van Santen, R. A. Catal. Today 2011, 171, 168.

(20) Geerlings, J. J. C.; Wilson, J. H.; Kramer, G. J.; Kuipers, H. P. C. E.; Hoek, A.; Huisman, H. M. Appl. Catal., A 1999, 186, 27.

(21) Ciobica, I. M.; van Santen, R. A. J. Phys. Chem. B 2003, 107, 3808.

(22) Ge, Q.; Neurock, M. J. Phys. Chem. B 2006, 110, 15368.

(23) Filot, I. A. W.; Shetty, S. G.; Hensen, E. J. M.; van Santen, R. A. J. Phys. Chem. C 2011, 115, 14204.

(24) Lanzani, G.; Nasibulin, A. G.; Laasonen, K.; Kauppinen, E. I. Nano Res. 2009, 2, 660.

(25) Kruse, N.; Schweicher, J.; Bundhoo, A.; Frennet, A.; de Bocarmé, T. V. Top. in Catal. 48 2008, 145.

(26) Inderwildi, O. R.; Jenkins, S. J.; King, D. A. J. Phys. Chem. C 2008, 112, 1305.

(27) Blyholder, G.; Lawless, M. Langmuir 1991, 7, 140.

(28) Zhuo, M. K.; Tan, K. F.; Borgna, A.; Saeys, M. J. Phys. Chem. C 2009, 113, 8357.

(29) Elahifard, M. R.; Jigato, M. P.; Niemantsverdriet, J. W. ChemPhysChem 2012, 13, 89.

(30) Deng, L. J.; Huo, C. F.; Liu, X. W.; Zhao, X. H.; Li, Y. W.; Wang, J.; Jiao, H. J. Phys. Chem. C 2010, 114, 21585.

(31) Elahifard, M. R.; Jigato, M. P.; Niemantsverdriet, J. W. Chem. Phys. Lett. 2012, 534, 54.

(32) Iglesia, E.; Reyes, S. C.; Madon, R. J.; Soled, S. L. Adv. Catal. 1993, 39, 221.

(33) Ciobica, I. M.; Kramer, G. J.; Ge, Q.; Neurock, M.; van Santen, R. A. J. Catal. 2002, 212, 136.

(34) Bridge, M. E.; Comrie, C. M.; Lambert, R. M. Surf. Sci. 1977, 67, 393.

(35) Pfnür, H.; Feulner, P.; Menzel, D. J. Chem. Phys. 1983, 79, 4613.

(36) Williams, E. D.; Weinberg, W. H. Surf. Sci. 1979, 82, 93.

(37) Tao, F.; Dag, S.; Wang, L. W.; Liu, Z.; Butcher, D. R.; Bluhm, H.; Salmeron, M.; Somorjai, G. A. Science 2010, 327, 850.

(38) Dalla Betta, R. A. J. Phys. Chem. 1975, 79, 2519.

(39) Kobayashi, M.; Shirasaki, T. J. Catal. 1973, 28, 289.

(40) Kobayashi, M.; Shirasaki, T. J. Catal. 1974, 32, 254.

(41) Calderazzo, F.; L'Eplattenier, F. Inorg. Chem. 1967, 6, 1220.

(42) Kresse, G.; Hafner, J. Phys. Rev. B: Condens. Matter Mater. Phys. 1994, 49, 14251.

(43) Kresse, G.; Furthmüller, J. Phys. Rev. B: Condens. Matter Mater. Phys. 1996, 54, 11169.

(44) Kresse, G.; Furthmüller, J. Comput. Mater. Sci. 1996, 6, 15.

(45) Hammer, B.; Hansen, L. B.; Nørskov, J. K. Phys. Rev. B: Condens. Matter Mater. Phys. 1999, 59, 7413.

(46) Vanderbilt, D. Phys. Rev. B: Condens. Matter Mater. Phys. 1990, 41, 7892.

(47) Jennison, D. R.; Schultz, P. A; Sears, M. P. J. Chem. Phys. 1997, 106, 1856.

(48) King, H. W. in CRC Handbook of Chemistry and Physics, Lide, D. R., Frederikse, H. P. R., Eds.; CRC Press: Boca Raton, 1996; pp 12–18.

(49) Iglesia, E. Appl. Catal., A 1997, 161, 59.

(50) Henkelman, G.; Uberuaga, B. P.; Jonsson, H. J. J. Chem. Phys. 2000, 113, 9901.

(51) Henkelman, G.; Jonsson, H. J. J. Chem. Phys. 2000, 113, 9978.

(52) Henkelman, G.; Jonsson, H. J. J. Chem. Phys. 1999, 111, 7010.

(53) Soled, S. L.; Malek, A.; Miseo, S.; Baumgartner, J.; Kliewer, C.; Afeworki, M.; Stevens, P. A. Stud. Surf. Sci. Catal. 2006, 162, 103.

(54) Mirth, G.; Eder, F.; Lercher, J. A. Appl. Spectrosc. 1994, 48, 14251.

(55) Gajdos, M.; Eichler, A.; Hafner, J. J. Phys.: Condens. Matter 2004, 16, 1141.

(56) Thomas, G. E.; Weinberg, W. H. J. Chem. Phys. 1979, 70, 1437.

(57) Brodén, G.; Gafner, G.; Bonzel, H. P. Surf. Sci. 1979, 84, 295.

(58) Kleis, J.; Greeley, J.; Romero, N. A.; Morozov, V. A.; Falsig, H.; Larsen, A. H.; Lu, J.; Mortensen, J. J.; Dulak, M.; Thygesen, K. S.; Norskov, J. K.; Jacobson, K. W. Catal. Lett. 2011, 141, 1067.

(59) Föhlisch, A.; Nyberg, M.; Hasselström, J.; Karis, O.; Pettersson, L. G. M.; Nilsson, A. Phys. Rev. Lett. 2000, 85, 3309.

(60) Blyholder, G. J. Chem. Phys. 1964, 68, 2772.

(61) Mager-Maury, C.; Bonnard, G.; Chizallet, C.; Sautet, P.; Raybaud, P. ChemCatChem 2011, 3, 200.

(62) Dumesic, J. A.; Rudd, D. F.; Aparicio, L. M.; Rekoske, J. E. Treviño, A A. The Microkinetics of Heterogeneous Catalysis; American Chemical Society: Washington, D.C., 1993.

(63) Yokomizo, G. H.; Louis, C.; Bell, A. T. J. Catal. 1989, 120, 1.

6120

dx.doi.org/10.1021/ja311848e | J. Am. Chem. Soc. 2013, 135, 6107–6121

(64) Chin, S. Y.; Williams, C. T.; Amiridis, M. D. *J. Phys. Chem. B* **2006**, *110*, 871.

(65) Boudart, M.; Djéga-Mariadassou, G. *Kinetics of Heterogeneous Catalytic Reactions*; Princeton University Press: Princeton, N.J., 1984.

(66) Pedrero, C.; Waku, T.; Iglesia, E. *J. Catal.* **2005**, *233*, 242.

(67) Das, T. K.; Jacobs, G.; Davis, B. H. *Catal. Lett.* **2005**, *101*, 187.

(68) van Berge, P. J.; Everson, R. C. *Stud. Surf. Sci. Catal.* **1997**, *107*, 207.

(69) Madon, R. J.; Iglesia, E. *J. Catal.* **1994**, *149*, 428.

(70) Crabtree, R. *The Organometallic Chemistry of Transition Metals*; John Wiley & Sons: Hoboken, N.J., 2005.

(71) Quicksall, C. O.; Spiro, T. G. *Inorg. Chem.* **1968**, *7*, 2365.

(72) Yates, J. T.; Duncan, T. M.; Worley, S. D.; Vaughan, R. W. *J. Chem. Phys.* **1979**, *70*, 1219.

(73) Cavanagh, R. R.; Yates, J. T. *J. Chem. Phys.* **1981**, *74*, 4150.

(74) Frank, M.; Bäumer, M. *Phys. Chem. Chem. Phys.* **2000**, *2*, 3723.

(75) Scheffler, M. *Surf. Sci.* **1979**, *81*, 562.

(76) Olsen, C. W.; Masel, R. I. *Surf. Sci.* **1988**, *201*, 444.

(77) Kellner, C. S.; Bell, A. T. *J. Catal.* **1981**, *70*, 418.

(78) Krishnamoorthy, S.; Tu, M.; Ojeda, M. P.; Pinna, D.; Iglesia, E. *J. Catal.* **2002**, *211*, 422.

(79) Dry, M. E. *Appl. Catal., A* **1996**, *138*, 319.

(80) Ponec, V. *Catal. Today* **1992**, *12*, 227.

(81) Outi, A.; Rautavuoma, I.; van der Baan, H. S. *Appl. Catal* **1981**, *1*, 247.

(82) Eliason, S. A.; Bartholomew, C. H. *Appl. Catal., A* **1999**, *186*, 229.

(83) Reymond, J. P.; Meriaudeau, P.; Pommier, B.; Bennett, C. O. *J. Catal.* **1980**, *64*, 163.

(84) Visconti, C. G.; Tronconi, E.; Lietti, L.; Forzatti, P.; Rossini, S.; Zennaro, R. *Top. Catal.* **2011**, *54*, 786.

(85) Davis, B. H. *Catal. Today* **2009**, *141*, 25.

(86) Hall, W. K.; Kokes, R. J.; Emmett, P. H. *J. Am. Chem. Soc.* **1960**, *82*, 1027.

6121

dx.doi.org/10.1021/ja311848e | *J. Am. Chem. Soc.* 2013, 135, 6107−6121